CrossMark

# Single point incremental forming of AA6061 thin sheet: calibration of ductile fracture models incorporating anisotropy and post forming analyses

Shamik Basak [1] · K. Sajun Prasad [1] · Ajay M. Sidpara [1] · Sushanta Kumar Panda [1]

## Abstract

Nowadays, single point incremental forming (SPIF) process is gaining popularity for fabrication of various asymmetrical intricate sheet metal components in automobile, aerospace, ship-building, additive manufacturing and also in biomedical sectors. In the present work, a SPIF set up was designed and developed in-house to perform forming experiments using AA6061 thin sheet material. The fracture forming limit diagram (FFLD) was assessed experimentally using punch stretching test, and it was validated with the optimized SPIF test data. Further, an effort was made to modify the existing seven damage models implementing Hill48 anisotropy plasticity theory. Consequently, the effective plastic strains at the onset of fracture were predicted and compared with experimental data. All the critical damage parameters of investigated ductile fracture models were successfully calibrated using uniaxial tensile test data, and the theoretical FFLD was also estimated incorporating the anisotropy plasticity theory. Among the seven damage models, the Bao-Wierzbicki (BW) damage model was found to be the most efficient damage model with an average absolute error of 2.71%. Additionally, the influence of sheet metal anisotropy on the effective fracture strain was studied by comparing the fracture strain in 2D ($\eta$, $L_P$) and 3D ($\eta, L_P, \overline{\varepsilon}_f$ ) fracture locus. In order to get insight into forming behaviour and surface roughness, the microstructural examination on the truncated dome fabricated using optimised parameters was carried out through micro texture analyses.

## Introduction

In recent times, sheet metal forming industries are showing immense interest in single point incremental forming (SPIF) process due to its high degree of flexibility in part design, huge reduction in tooling cost and enhanced formability. In this process, the thin sheet metal is rigidly clamped and deformed progressively into the desired shape by localized plastic deformation using a rigid forming tool [1]. The simple or complex tool path can be easily planned through a CNC machine tool, and any modification in the final shape can be instantly incorporated by controlling the motion of the tool [2]. Moreover, a multi-step tool path strategy was often adapted to increase the inclination of the wall angles of the formed component [3]. This flexible and die-less nature make the process more suitable for prototyping and fabrication of highly intricate 3D-shapes. However, due to high production time, the SPIF process cannot be used for the mass production of the industrial components. Rather, the SPIF process is efficiently adapted for small sized batch or customized production and rapid prototyping of metallic parts. The widespread application of incrementally formed components ranges from different industries such as

✉ Sushanta Kumar Panda
  sushanta.panda@mech.iitkgp.ernet.in

1   Department of Mechanical Engineering, Indian Institute of
    Technology Kharagpur, Kharagpur, West Bengal 721302, India

automobile, aerospace, shipping, and biomedical. The incremental forming process is gaining popularity to produce door hoods and car fenders in auto bodies, hydraulic doors for Airbus, composite pressure vessel mould [3] etc. More recently, SPIF process is used to fabricate various custom-made biomedical implants for knee arthroplasty and also complex shaped cranial implant [4]. However, several researchers indicated that the formability of incrementally formed product is affected by several factors such as material properties, tool design, lubricant condition, tool path etc. Hence, different optimization techniques such as the design of experiments (DOE), genetic algorithm (GA), response surface methodology (RSM) etc. were proposed to optimize the SPIF process [5].

Maximum workability during sheet metal forming operation is often characterized by indulging the forming limit diagram (FLD) concept to detect the diffuse/ localized necking condition followed by a fracture phase. However, using FLD as a forming limit always leads to an erroneous prediction of the formability of a SPIF component. This is due to the fact that the maximum formability of the sheet metal components produced during SPIF process is limited by fracture due to suppression of the localized necking. Hence, it is always useful to determine the fracture limit to predict the maximum formability during SPIF process. Depending on crack opening modes along different strain paths, the fracture limit can be broadly classified into two categories i.e. tensile fracture forming limit diagram and shear fracture forming limit diagram. Tensile fracture forming limit diagram or fracture forming limit diagram (FFLD) is attributed due to the appearance of tensile cracks into the sheet metal during SPIF process and traditional forming process. Whereas, shear fracture forming limit locus (SFFL) was generated from in-plane shear cracks observed during torsion and in-plane shear tests as shown by Isik et al. [6]. Experimental FFLD was constructed by Isik et al. [6] using different sheet formability tests such as bulge tests, dome tests and Nakazima tests for achieving different strain paths for AA1050-H111 sheet metal. Later, the experimental FFLD was validated with the SPIF test results. Further, the fracture loci in metal forming were characterized by Martins et al. [7] indulging various crack opening modes I, II and III.

Theoretical FFLD can be predicted coupling the fundamental knowledge of plane stress based plasticity theory with the continuum damage models during various crack separation modes. Recently, sheet metal forming researchers are interested in utilising different ductile fracture models to assess the theoretical fracture limit. These fracture models can be classified into three broad categories, namely, empirical models, phenomenological models, and physics based models [8, 9]. In empirical models, relationships are established using experimental fracture strain data. The fracture strain in phenomenological model is estimated through the various assumptions imposed on the stress-strain relationship. Physics based models are based on the modeling of the micro void initiation and growth, which is followed by the coalescence [10]. These damage models require few destructive tests for calibration of the critical fracture parameters. Habibi et al. [8] used twenty-two different ductile and shear fracture models to predict the forming limit for TWIP steel during stretch forming operation. Bai and Wierzbicki [10] conducted an extensive comparative analyses to determine the 3D fracture locus of sixteen different damage models, and these were calibrated for TRIP690, TRIP780, and AA2024-T351 sheet metals. All the theoretical FFLD prediction till discussed had not considered the anisotropy within the sheet metal. Recently, Park et al. [11] imposed the Hill48 anisotropic model into Lou damage model to predict the fracture behaviour of three anisotropic sheet metal at different sheet orientations. Isik et al. [6] incorporated the normal anisotropy of AA1050-H111 sheet metal into Ayada damage model to predict FFLD theoretically. However, it is evident from the literature studies that a relatively scarce amount of research was conducted on the ductile fracture model of SPIF process. Moreover, there is no open literature where the anisotropy in sheet metal is incorporated to calibrate the available fracture models in the context of SPIF process.

In past, few post-deformation studies had shown that during the incremental forming process the unconstrained metal surfaces tends to roughen when sheet metal is subjected to large plastic deformation [12]. Surface roughness is one of the crucial parameters in a post-formed product which can act as beneficiary or hindrance based on the requisite application. The surface roughness represents a better environment for cell growth [13] in biomedical application whereas, it not only affects the appearance but also seriously affects its service life which may lead to catastrophic failure of the structure [14] in aerospace application. In this context, the effect of texture on formability improvement and surface roughness in SPIF process has not been investigated till date. In the present work, the optimized SPIF process parameter was used to produce conical cups implementing in-house developed SPIF test setup. The punch stretching tests have conducted to determine the fracture limit, and the optimized SPIF test data were used to validate the estimated experimental FFLD. Also, the FFLD was predicted theoretically implementing Hill48 anisotropy plasticity theory in seven different

fracture models, and the critical damage parameters of each fracture model were calibrated using the uniaxial tensile test data and anisotropy value of the sheet metal. The predictive accuracy of each fracture model was compared along six different strain paths. The texture analysis was conducted to get insight into the formability improvement during SPIF process and surface roughness of post deformed cups.

# Fracture models

## Hill48 anisotropy yield function

Hill48 [15] quadratic material model was used to describe the anisotropic evolution of the investigated aluminum sheet material. The generalized expression for anisotropic Hill48 yield model is defined as per Eq. (1).

$$\overline{\sigma}_H(\sigma_{ij}) = \sqrt{F(\sigma_{yy}\text{-}\sigma_{zz})^2 + G(\sigma_{zz}\text{-}\sigma_{xx})^2 + H(\sigma_{xx}\text{-}\sigma_{yy})^2 + 2L\sigma_{yz}^2 + 2M\sigma_{zx}^2 + 2N\sigma_{xy}^2} \tag{1}$$

Here, $\overline{\sigma}_H$ is the effective plastic stress evaluated through Hill48 yield model, and $F$, $G$, $H$, $L$, $M$ and $N$ are the anisotropic material constants. For simplicity, only normal anisotropy within the sheet material ($r_0 = r_{45} = r_{90} = r = \overline{r}$ and $\sigma_0 = \sigma_{45} = \sigma_{90} = \sigma$) was considered in this work. Here, $\overline{r}$ is defined as normal anisotropy, and the same is defined as, $\overline{r} = (r_0 + 2r_{45} + r_{90})/4$. It is noteworthy to mention that if the value of the normal anisotropy is unity i.e. $r_0 = r_{45} = r_{90} = r = \overline{r} = 1$, then the Hill48 model reduces to von Mises (VM) isotropic yield function. Further, applying associative flow rule in Eq. (1), the anisotropy coefficients were determined, and the same is defined by Eq. (2).

$$H = \frac{r}{1+r}, \quad G = \frac{1}{1+r} \quad \frac{F}{H} = \frac{1}{r} \quad \text{and} \quad N = \frac{1+2r}{1+r} \tag{2}$$

It was assumed that the anisotropic orientation of sheet metal coincided with the principal direction of stress tensor i.e. $\sigma_{xx} = \sigma_1$ and $\sigma_{yy} = \sigma_2$. Incorporating plane stress condition ($\sigma_{zz} = \sigma_{zx} = \sigma_{yz} = 0$) in Eq. (1) and using Eq. (2), the Hill48 yield model is simplified as shown in Eq. (3).

$$\overline{\sigma}_H(\sigma_{ij}) = \sqrt{\sigma_1^2 - \frac{2r}{1+r}\sigma_1\sigma_2 + \sigma_2^2} \tag{3}$$

Here, $\sigma_1$ and $\sigma_2$ ($\sigma_1 \geq \sigma_2$) are the first and second principal stress component of the stress tensor ($\sigma$) respectively. The Lankford anisotropy parameter ($r$-value) and the yield strength of the material was evaluated along rolling direction (RD) of the sheet metal. Upon simplification, Eq. (3) can be rewritten in the form of $\xi$ as shown in Eq. (4). Where, $\xi$ is

defined as the ratio of effective stress ($\overline{\sigma}_H$) to the first principal or major stress ($\sigma_1$).

$$\xi = \frac{\overline{\sigma}_H}{\sigma_1} = \sqrt{\alpha^2 - \frac{2r}{1+r}\alpha + 1} \tag{4}$$

Associative flow rule [16, 17] was applied to evaluate the associated plastic strain increment, and upon further simplification, the strain ratio ($\rho = \varepsilon_2/\varepsilon_1$, $\varepsilon_1 \geq \varepsilon_2$) can be represented in the form of stress ratio ($\alpha = \sigma_2/\sigma_1$, $\sigma_1 \geq \sigma_2$) as shown in Eq. (5).

$$\rho = \frac{d\varepsilon_2}{d\varepsilon_1} = \frac{\alpha(1+r)-r}{1+r-r\alpha} \tag{5}$$

The effective strain was evaluated from the expression of total plastic work, and further simplified by implementing the values of $\rho$, $\alpha$ and $\xi$ as shown in Eq. (6).

$$\overline{\varepsilon} = \frac{\varepsilon_1(1+\rho\alpha)}{\xi} = \left(\frac{1+r}{\sqrt{1+2r}}\right)\sqrt{\varepsilon_1^2 + \frac{2r}{1+r}\varepsilon_1\varepsilon_2 + \varepsilon_2^2} \tag{6}$$

## Characterization of 3D stress state in the anisotropic triaxiality space of ($\eta_H, L_P, \overline{\sigma}_H$)

The generalized stress state of a material can be characterized by two non-dimensional parameters, stress triaxiality ratio ($\eta$) and Lode parameter ($L_P$). Incorporating Hill48 anisotropic model, the stress triaxiality ($\eta_H$) of a material is defined as shown in Eq. (7).

$$\eta_H = \frac{\sigma_m}{\overline{\sigma}_H} = \frac{\sigma_{xx} + \sigma_{yy} + \sigma_{zz}}{3\sqrt{F(\sigma_{yy}\text{-}\sigma_{zz})^2 + G(\sigma_{zz}\text{-}\sigma_{xx})^2 + H(\sigma_{xx}\text{-}\sigma_{yy})^2 + 2L\sigma_{yz}^2 + 2M\sigma_{zx}^2 + 2N\sigma_{xy}^2}} \tag{7}$$

Here, $\sigma_m = (\sigma_{xx} + \sigma_{yy} + \sigma_{zz})/3$ represents the hydrostatic stress component, and it accounts the volume change and does not contribute in the plastic deformation of a material.

Recently, Park et al. [11] used the tensor transformation to show the anisotropic influence of a loading state on different material orientations. Correspondingly, they derived

analytical relations incorporating Hill48 anisotropic model into the stress triaxiality expression. However, in this work, it was already mentioned that the maximum principal stress ($\sigma_1$) is acting along the RD of the sheet metal. Hence, using the formulation proposed by Park et al. [11], $\eta_H$ can be expressed in terms of maximum principal stresses (assuming $\sigma_1 \geq \sigma_2 \geq \sigma_3$) as shown in Eq. (8).

$$\eta_H = \frac{\sigma_1 + \sigma_2 + \sigma_3}{3\sqrt{(\sigma_1-\sigma_3)^2 \cdot S}} \tag{8}$$

Where, $S = F\left(\frac{1+L_P}{2}\right)^2 + G + H\left(\frac{1-L_P}{2}\right)^2$ and $L_P = \frac{2\sigma_2-\sigma_1-\sigma_3}{\sigma_1-\sigma_3}$

Here, $L_P$ is the Lode parameter which can be defined in principal stress space. The value of $L_P$ ($-1 \leq L_P \leq 1$) is 1, 0 and $-1$ for axisymmetric compression, plane strain or generalized shear loading and axisymmetric tension condition respectively [10].

Further, the stress state at a point can be represented in the Cartesian coordinate system of principal stresses, cylindrical coordinate system and spherical coordinate system as proposed by Bai and Wierzbicki [18] and the same is depicted in Fig. 1. In the figure, $\overrightarrow{OA}$ represents a general stress vector in Cartesian coordinate system, and it is decoupled into two perpendicular vectors. One of the components is $\overrightarrow{OO'} = \sqrt{3}\sigma_m$, which represents the hydrostatic stress component. Another vector $\overrightarrow{O'B}$ is lying in the deviatoric plane. Park et al. [11] also showed analytically
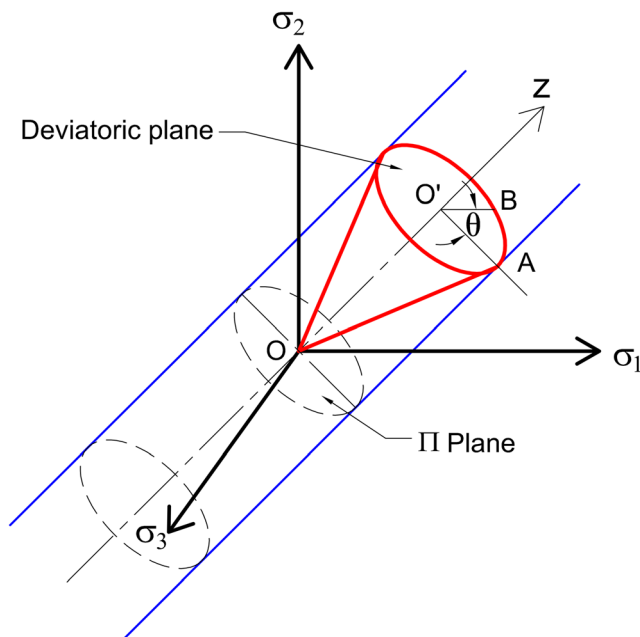
that the principal stresses could be expressed in the ($\eta_H$, $L_P$) space as shown in Eq. (9).

$$\sigma_1 = \left\{\eta_H + \frac{3-L_P}{6\sqrt{S}}\right\}\overline{\sigma}_H,$$
$$\sigma_2 = \left\{\eta_H + \frac{2L_P}{6\sqrt{S}}\right\}\overline{\sigma}_H \text{ and } \sigma_3 = \left\{\eta_H - \frac{3+L_P}{6\sqrt{S}}\right\}\overline{\sigma}_H \tag{9}$$

The transformation from the principal plastic strain coordinate ($\varepsilon_1$, $\varepsilon_2$) to triaxiality space ($\eta_H$, $L_P$) was carried out using the above relations and Hill48 anisotropic yield criterion as discussed in next subsection.

## Ductile fracture criteria

In this work, two empirical damage models (Bao-Wierzbicki and constant thickness strain based FFLD), four phenomenological damage models (Clift, Cockcroft-Latham, Oh, and Brozzo) and one physical based damage model (Rice-Tracey) were considered. Moreover, the anisotropy effect of the sheet material was considered in the analytical prediction of the fracture strain. Subsequently, Hill48 anisotropic yield theory was utilized to modify the above mentioned ductile damage models and the mathematical formulations of each model are discussed in detail below.

### Bao-Wierzbicki (BW) damage criterion

Bao and Wierzbicki [19] conducted an extensive experimental study on the AA2024-T351 material to evaluate the effective fracture strain ($\overline{\varepsilon}_f$) locus over a wide triaxiality range of axisymmetric tension to compression. From the experimental results, they concluded that the fracture locus is not a continuous monotonic function of stress triaxiality, rather they proposed that the fracture locus could be branched into three distinct regions with three different empirical relations. However for sheet metal forming operation, $\overline{\varepsilon}_f$ and stress triaxiality is related to each other through a parabolic relationship as shown in Eq. (10).

$$\overline{\varepsilon}_f = \frac{b}{3\eta_H} \tag{10}$$

Clearly, it is evident from Eq. (10) that $b = \overline{\varepsilon}_f$ during uniaxial tensile test $\left(\eta_H = \frac{1}{3}\right)$. Again, the critical damage parameter of BW model can be represented as per Eq. (11).

$$C_{BW} = \int_0^{\overline{\varepsilon}_f} \frac{\sigma_m}{\overline{\sigma}_H} d\overline{\varepsilon} \tag{11}$$



**Fig. 1** Geometrical representation of the coordinate system in principal stress space

In this work, a detailed mathematical analysis was carried out with BW fracture criterion incorporating Hill48 anisotropic yield model to evaluate $C_{BW}$ using uniaxial tensile test data. Strain path during the uniaxial tensile test could be correlated with the anisotropy value of the sheet metal, and the strain ratio could be derived from volume constancy theorem as $\rho = -\frac{r}{1+r}$. The strain path up to fracture of a tensile specimen could be divided into three piecewise linear segments as proposed by Lee [20]. Accordingly, the complete strain path (0–3) was subdivided into three linear segments, 0–1, 1–2 and 2–3 as shown in Fig. 2. Point 1, 2 and 3 corresponds to the onset of diffuse necking, localized necking and fracture location respectively. It was proposed that up to diffuse and localized necking the major strain equals to $n$ and $2n$ respectively, i.e. $\varepsilon_{1d} = n$ and $\varepsilon_{1l} = 2n$ (here, $n$ corresponds to strain hardening exponent of the material as per Hollomon power hardening law, i.e. $\overline{\sigma} = K\overline{\varepsilon}^n$ ) [20, 21]. It is proposed by several researchers [6, 22] that the plane strain condition ($\rho = 0$) prevails up to fracture after localized necking. Imposing these boundary conditions, the strain and stress ratio for a different segment of the uniaxial strain path can be represented as per Eq. (12).

$$
\begin{aligned}
&\text{Up to } 0{-}1: \rho = -\frac{r}{1+r}, \quad \alpha = 0\\
&\text{Up to } 1{-}2: \rho = -\frac{r}{1+r}, \quad \alpha = 0\\
&\text{Up to } 2{-}3: \rho = 0, \quad \alpha = \frac{r}{1+r}
\end{aligned} \quad (12)
$$

Hence Eq. (11) can be modified using different ratio defined in Eqs. (4) and (6). Moreover, the integration
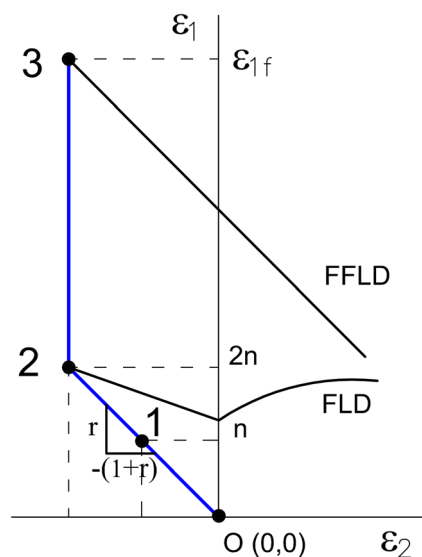


**Fig. 2** Typical strain path up to fracture during a uniaxial tensile test

was performed segment wise for three different boundary conditions. The final form of $C_{BW}$ is shown in Eq. (13).

$$
\begin{aligned}
C_{BW} &= \int_0^{\overline{\varepsilon}_{1f}} \frac{\sigma_m}{\sigma_1} \cdot \frac{\sigma_1}{\overline{\sigma}_H} \cdot \frac{d\overline{\varepsilon}}{d\overline{\varepsilon}_1} \, d\overline{\varepsilon}_1 = \int_0^{\overline{\varepsilon}_{1f}} \frac{1+\alpha}{3} \cdot \frac{1}{\xi} \cdot \frac{1+\rho\alpha}{\xi} \, d\overline{\varepsilon}_1\\
&= \int_0^{\overline{\varepsilon}_{1d}} \frac{(1+\alpha)(1+\rho\alpha)}{3\xi^2} \, d\overline{\varepsilon}_1 + \int_{\overline{\varepsilon}_{1d}}^{\overline{\varepsilon}_{1l}} \frac{(1+\alpha)(1+\rho\alpha)}{3\xi^2} \, d\overline{\varepsilon}_1 \quad (13)\\
&\quad + \int_{\overline{\varepsilon}_{1l}}^{\overline{\varepsilon}_{1f}} \frac{(1+\alpha)(1+\rho\alpha)}{3\xi^2} \, d\overline{\varepsilon}_1
\end{aligned}
$$

Imposing boundary conditions (Eq. (12)), the critical damage factor ($C_{BW}$) can be expressed in terms of major principal fracture strain ($\varepsilon_{1f}$) as shown in Eq. (14).

$$
C_{BW} = \left(\frac{1+r}{3}\right)\varepsilon_{1f} + 2n\left(\frac{r}{3}\right) \quad (14)
$$

In practical, it is very difficult to evaluate the major principal fracture strain ($\varepsilon_{1f}$) experimentally from the circular grid analysis (CGA) method. It has been mentioned in the literature that the direct measurement of the $\varepsilon_{1f}$ using CGA method led to an erroneous result due to inhomogeneous plastic deformation at the neighbourhood of the crack [23]. Hence, $\varepsilon_{1f}$ can be represented in the form of effective fracture strain ($\overline{\varepsilon}_f$) as shown in Eq. (6). Further simplifying and imposing boundary conditions the final form $\overline{\varepsilon}_f$ can be obtained as shown in Eq. (15).

$$
\overline{\varepsilon}_f = \left(\frac{1+r}{\sqrt{1+2r}}\right)\varepsilon_{1f} + 2n\left(1 - \frac{1+r}{\sqrt{1+2r}}\right) \quad (15)
$$

Again, the critical damage factor ($C_{BW}$) can also be evaluated by measuring the initial ($t_0$) and final thickness ($t_f$) of the fractured uniaxial tensile sample as per the mathematical relationship, $C_{BW} = \frac{2}{3}\ln\left(\frac{t_0}{t_f}\right)$, suggested by Lee [20]. Further using Eqs. (14) and (15); the unknown parameter $b$ can be evaluated as shown in Eq. (16).

$$
b = \overline{\varepsilon}_f = \frac{2}{\sqrt{1+2r}}\ln\left(\frac{t_0}{t_f}\right) + 2n\left(1 - \frac{1}{\sqrt{1+2r}}\right) \quad (16)
$$

From Eq. (10), it is evident that the fracture locus predicted by BW damage criterion is independent of the Lode parameter ($L_P$).

## Constant thickness strain based fracture forming limit diagram (CTFFLD)

CTFFLD model is based on the volume constancy theorem with an assumption that the thickness strain is constant [20]. CTFFLD is only valid during plane stress operation. The mathematical expression for CTFFLD is shown in Eq. (17).

The constant term ($C_{CTFFLD}$) of the straight line is evaluated from the through thickness principal strain at fracture point ($\varepsilon_{3f}$) value as shown in Eq. (17). Here the term with $0$ and $f$ as subscript represents the initial and final condition respectively.

$$\varepsilon_{1f} + \varepsilon_{2f} = -\varepsilon_{3f} = \ln\left(\frac{t_0}{t_f}\right) = C_{CTFFLD} \tag{17}$$

### Clift (CF) damage criterion

Freudenthal [24] proposed a damage model based on generalized plastic work. Later, Clift et al. [25] performed a considerable number of experiments and reported that fracture initiated when the plastic work per unit volume reached the critical damage value as shown in Eq. (18).

$$C_{CF} = \int_0^{\bar{\varepsilon}_f} \bar{\sigma}_H d\bar{\varepsilon} \tag{18}$$

Coupling power hardening law in Eq. (18) and further solving, the final form of the critical damage factor ($C_{CF}$) was evaluated according to Eq. (19).

$$\bar{\varepsilon}_f = \left[ C_{CF} \times \frac{n+1}{K} \right]^{\left(\frac{1}{n+1}\right)} \tag{19}$$

Clearly, the fracture locus predicted by Clift damage criterion is independent of stress triaxiality ratio ($\eta_H$) and Lode parameter ($L_P$).

### Cockcroft-Latham (CL) damage criterion

Cockcroft and Latham damage model [26] initially developed for forging operation. Later this model has been applied for sheet metal forming operation as shown by Tarigopula et al. [27]. Cockcroft and Latham [26] proposed that the ductile fracture often take place in the region of maximum tensile stress $\sigma_1$ as given by Eq. (20).

$$C_{CL} = \int_0^{\bar{\varepsilon}_f} \sigma_1 d\bar{\varepsilon} \tag{20}$$

Using Hollomon hardening law in Eq. (20), the fracture locus can be represented as per Eq. (21).

$$\bar{\varepsilon}_f = \left[ C_{CL} \times \frac{n+1}{K} \times \frac{6\sqrt{S}}{3 - L_P + 6\eta_H\sqrt{S}} \right]^{\left(\frac{1}{n+1}\right)} \tag{21}$$

The fracture locus predicted by CL damage criterion is dependent on both the stress triaxiality ratio ($\eta_H$) and Lode parameter ($L_P$).

### OH (OH) damage criterion

Oh et al. [28] proposed a modification of CL damage model to use it for the extrusion of AA2024 alloy and drawing of SAE 1144 cold-drawn steel. The damage model can be represented in normalized maximum principal stress as shown in Eq. (22).

$$C_{OH} = \int_0^{\bar{\varepsilon}_f} \frac{\sigma_1}{\bar{\sigma}_H} d\bar{\varepsilon} \tag{22}$$

Correspondingly, the fracture locus can be represented as shown in Eq. (23).

$$\bar{\varepsilon}_f = \left[ C_{OH} \times \frac{6\sqrt{S}}{3 - L_P + 6\eta_H\sqrt{S}} \right] \tag{23}$$

Oh damage model or modified CL model is also dependent on both the stress triaxiality ratio ($\eta_H$) and Lode parameter ($L_P$).

### Brozzo (BR) damage criterion

Brozzo et al. [29] altered the CL damage model by incorporating the hydrostatic stress component ($\sigma_m$) in the stress ratio, and the final form can be represented as per Eq. (24).

$$C_{BR} = \int_0^{\bar{\varepsilon}_f} \frac{2}{3} \frac{\sigma_1}{\sigma_1 - \sigma_m} d\bar{\varepsilon} \tag{24}$$

Using Eq. (9), the Eq. (24) can be further modified, and the fracture locus is represented in Eq. (25).

$$\bar{\varepsilon}_f = \left[ C_{BR} \times \frac{3}{2} \times \frac{3 - L_P}{3 - L_P + 6\eta_H\sqrt{S}} \right] \tag{25}$$

This criterion depends on both stress triaxiality ratio ($\eta_H$) and Lode parameter ($L_P$).

### Rice-Tracey (RT) damage criterion

A semi-empirical relation was developed by Rice and Tracey [30] considering the spherical void growth in an infinite solid subjected to normal stresses. The proposed damage model can be represented as per Eq. (26).

$$C_{RT} = \int_0^{\bar{\varepsilon}_f} 0.283 \exp\left(\frac{3}{2} \frac{\sigma_1}{\bar{\sigma}_H}\right) d\bar{\varepsilon} \tag{26}$$

Further solving, the effective fracture strain can be expressed as per Eq. (27).

$$\overline{\varepsilon}_f = \left[ C_{RT} \times \frac{1}{0.283 \exp\left(\frac{3}{2}\eta_H\right)} \right] \qquad (27)$$

This criterion is only dependent on the stress triaxiality ratio ($\eta_H$).

### Calibration of critical damage parameters

Only one destructive test is required to estimate the critical damage values of these one parameter theoretical damage models. In this work, uniaxial tensile test data was used to calibrate the seven various damage parameters. Hollomon hardening law was fitted with the uniaxial test response, and subsequently, $n$ and $K$ value was evaluated and shown in "Single point incremental forming (SPIF) experiment" section. Moreover, the effective fracture strain ($\overline{\varepsilon}_f$) was estimated indulging Hill48 anisotropic yield theory. Consequently, all the respective critical damage factor was calculated using the numerical values of different evaluated parameters such as, $\eta_H$, $L_P$, $n$, $K$, $F$, $G$, $H$ and $\overline{\varepsilon}_f$. For example, $C_{BR}$ was calculated using the values $\eta_H = \frac{1}{3}$, $L_P = -1$, $n = 0.11$ and $\overline{\varepsilon}_f = 1$.22 as per Eq. (25). As the analytical expression for $\overline{\varepsilon}_f$ was evaluated using Hill48 yield theory, hence all the evaluated critical damage parameters were also a function of the anisotropy value of the sheet material. Numerical value of each damage parameters and a comparative study among the damage models are elaborately discussed in the "Prediction and validation of fracture locus of AA6061 sheet metal" section.

### Experiments to validate predicted fracture limit

In this work, punch stretching (PS) test was used to evaluate both the necking and fracture limit of the investigated sheet metal. The test is similar as that of the same proposed by Nakajima [31]. The PS test setup consisted of upper and lower die and a hemispherical punch of 50 mm diameter. A constant blank holding force of 15 bar was applied on the blank through a circular draw bead which restricted the material flow from the flange region. A detail of this test setup was reported elsewhere [32, 33], and the bending strain accumulated due to use of sub size punch was corrected using the method described in the previous literature [34]. In Nakazima tests [31], rectangular blanks with a fixed length and varying width are deformed using a hemispherical punch to achieve different strain paths. However, in this work, circular blanks with different recess diameter were used to avoid the draw-bead failure during deformation. In total, six different strain paths (SP1-SP6), ranging from tension-tension to tension-compression region were

designed by changing the geometry of the test specimens as shown in previous literature [32]. All the above specimens were tested in dry conditions whereas the 90 mm diameter specimen was tested in both dry and lubricated condition to achieve altogether six distinct strain paths. Before the experiment, blanks were imprinted with circular grid pattern of 2.5 mm diameter ($d_0$) using electrochemical etching process. After deformation, the deformed grids were measured along major ($d_1$) and minor ($d_2$) directions using stereo zoom microscope. Consequently, the principal surface strains induced in the specimens were calculated through circular grid analysis (CGA) method using the relationship, $\varepsilon_i = \ln(d_i/d_0)$. Where $i$=1 and 2 for major and minor direction respectively. Various fractured cups obtained for different strain paths are shown in Fig. 3a with the corresponding fracture location.

The experimental fracture strain ($\varepsilon_{1f}$, $\varepsilon_{2f}$) was estimated from the fracture cups resulted from PS operation. It is well established in the previous literature [22, 23, 34] that after localized necking there is no significant lateral staining of the material. Rather, fracture or splitting of the necked dome occurs along plane strain deformation path. Hence, second/ minor principal strain was estimated as $\varepsilon_{2f} = \varepsilon_{2n}$, where $\varepsilon_{2n}$ was the minor principal strain at necking which was easily evaluated experimentally through CGA. Third principal fracture strain was derived using the equation $\varepsilon_{3f} = \ln\left(\frac{t_f}{t_0}\right)$, where $t_0$ is the initial sheet thickness and $t_f$ is the fracture thickness or sometimes referred as the 'gauge length' by several researchers [6, 23]. To evaluate the fracture thickness ($t_f$), the fractured dome was cut perpendicular to the fracture line, and the fracture surface was observed under an optical microscope. The minimum perpendicular distances of the thinned cross-section of the leaf were measured. In Fig. 3b, two perpendicular distances of the fractured leaf, i.e. $t_{f1}$ and $t_{f2}$, are shown for a fracture specimen deformed along SP3 strain path. The minimum of these two distances is considered as the fracture thickness ($t_f$). Finally, first principal/major fracture strain ($\varepsilon_{1f}$) was estimated using constant volume constrains condition as per the Eq. (28). Thus, the evaluated fracture locus was used to plot the experimental fracture forming limit diagram (FFLD) as described in "Experimental fracture forming limit diagram" section.

$$(\varepsilon_{1f})_{SPi} = \left(\ln\frac{t_0}{t_f}\right)_{SPi} - (\varepsilon_{2f})_{SPi}, \quad i = 1, 2, \ldots, 6. \qquad (28)$$

### Single point incremental forming (SPIF) experiment

In the present study, AA6061 thin sheet metal with an average thickness of 0.7 mm was used. The uniaxial tensile test was
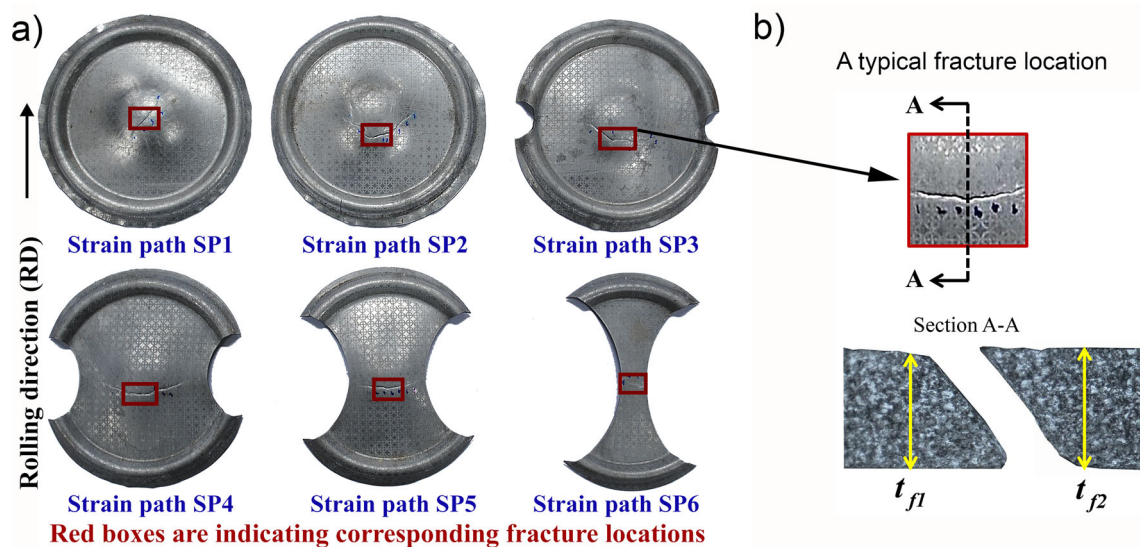
**Fig. 3** **a** Fractured cups along different loading paths and **b** fracture thickness measured along the through-thickness direction of the SP3 fractured sample

performed along rolling direction (RD) of the sheet metal with a crosshead velocity of 2 mm/min. Various mechanical responses such as yield strength (YS), total elongation till fracture (in %), ultimate tensile strength (UTS), strength coefficient ($K$-value), and strain hardening exponent ($n$-value) were evaluated from tensile test response. The Lankford anisotropy parameter ($r$-value) of the material along RD was also estimated from the tensile test data. Detailed procedure about tensile test and specimen geometry is discussed elsewhere [35, 36]. The consolidated mechanical responses of the AA6061 material are shown in Table 1.

## Development of experimental setup and tool path planning

A laboratory scale single point incremental forming (SPIF) test setup was conceptualized and indigenously developed to determine the fracture limit of the investigated sheet metal. The developed experimental setup with the tool workpiece combination is shown in Fig. 4a. The SPIF test setup consisted of a blank holder, backing plate and forming tool with the hemispherical tip of different diameter as depicted in Fig. 4c. The deformable sheet of 170 mm × 170 mm was clamped between blank holder and the backing support plate rigidly by means of 12 number of M6 bolts as shown schematically in Fig. 4b. The forming tool with cylindrical shank was attached to the main spindle of a 3-axis CNC milling machine (PCNC 1100 CNC mill) through a tool

holder (Fig. 4a). The tool was rotated about its own axis and also moved on the workpiece with a predefined tool path. Also, the amount of the step-down length of a forming tool after each pass is defined as step size. In this work, the tool path was designed with the commercial software MasterCAM. Initially, a considerable number of trial experiments were carried out to find out the feasibility and capability of the designed SPIF setup. Subsequently, a variable wall angle ($\psi$) was selected by considering an arc of a circle as generatrix to model an axisymmetric part. The spindle speed was kept constant at 2500 rpm throughout the SPIF operation. Also, the lubrication was performed on the blank before starting the tests. After rigorous trial experiments, the spiral tool path was adapted with a variable wall angle, and the final 3D shape of the tool path is depicted in Fig. 5a. The experiment was stopped when the visible crack/fracture was observed in the deformed dome. After experiments, the major and minor true strains on the deformed dome surface were measured through the CGA method. One typical model developed through MasterCAM software is compared with the experimental fractured truncated dome as shown in Fig. 5b and c respectively. It is noteworthy to mention that, SPIF tested dome was fractured directly without any exhibition of localized necking. Hence, the surface strain measured at the fracture point directly yielded the fracture strain on the principal strain axis.

Further, it was observed from the trial experiments that the input process parameters like forming tool diameter, vertical

**Table 1** Mechanical parameters for AA6061 sheet metal along rolling direction

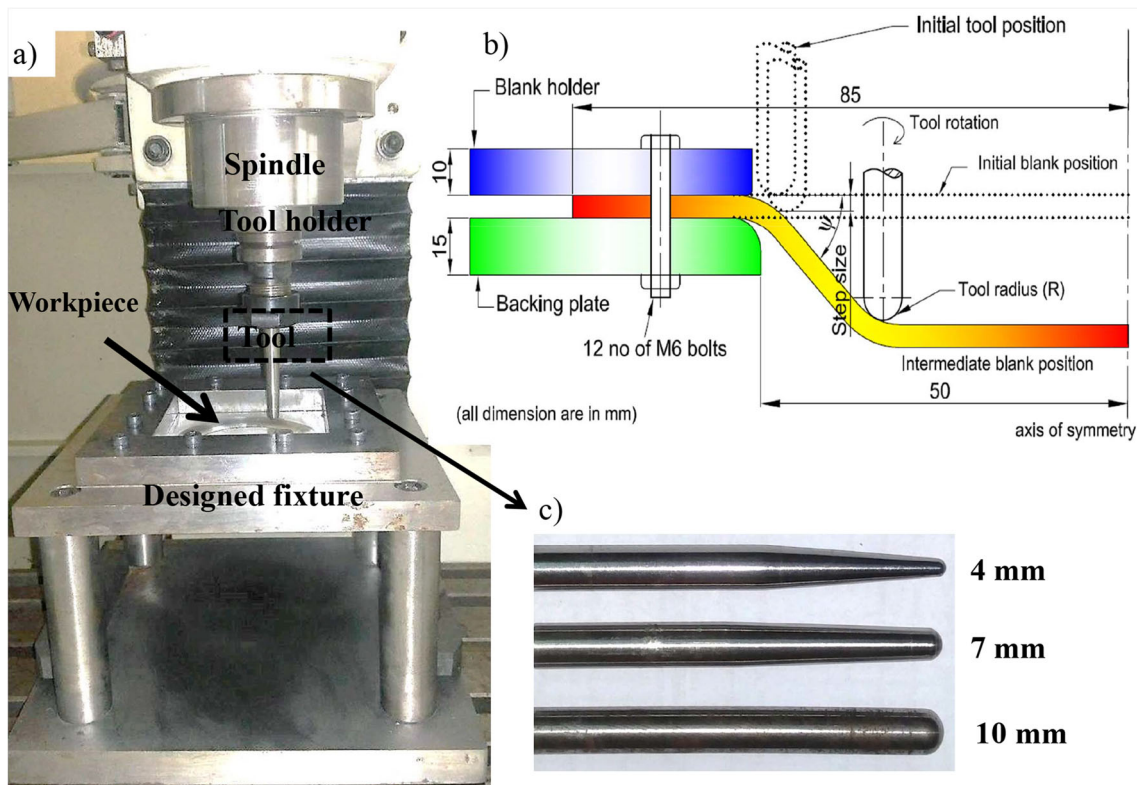| Yield strength (MPa) | UTS (MPa) | Total elongation | Lankford anisotropy coefficient ($r$) | Hollomon hardening law |
|---|---|---|---|---|
| 171.27 | 194.18 | 10% | 0.55 | $\sigma = 310.4\varepsilon^{0.11}$ |

**Fig. 4** **a** SPIF process experimental setup with tool workpiece combination, **b** schematic of experimental setup, and **c** forming tools with different hemispherical tool tip diameter used

step size and tool feed rate had a significant effect on the formability of the sheet metal which are in agreement with the literature [12, 37–39]. It was indicated that the formability during SPIF process depended upon the radius of the tool ($r_{tool}$) and the radius of the circular component ($r_{part}$) which was designed to be fabricated with the SPIF process [40, 41]. It was concluded that a small value of ($r_{part}/r_{tool}$) with a large tool radius ($r_{tool}$) led to failure of the sheet metal by fracture with a hint of localized necking. Whereas, a small tool diameter with a large value of the ratio ($r_{part}/r_{tool}$) led to the fracture of the sheet metal without any hint of localized necking. It was also observed that if the tool radius decreases then the formability increased. Moreover, for bigger tool diameter, the tool-workpiece contact zone is bigger which increases the amount of contact forces. On the other hand, for smaller tool diameter, there is a highly concentrated deformation zone which causes

high strain accumulation and leads to better formability. It was found that if the step size was increased then the surface roughness increased, and also the formability of the component reduced significantly due to large plastic deformation. Similarly, increasing feed rate reduced the process time but unfortunately, formability was also reduced. Hence, it is necessary to optimise the input process parameters before using the SPIF results further for fracture limit analysis. Consequently, the optimization of the SPIF process was carried out through a statistical tool, response surface methodology (RSM), as discussed in next section.

## SPIF process optimisation

It has been reported in previous literature that the surface of the sheet gets roughen with the increase in the plastic strain
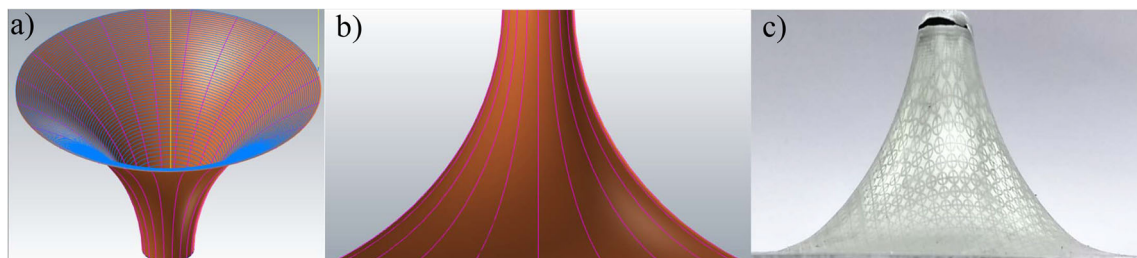


**Fig. 5** **a** Adopted 3D tool path in the present work and comparison of the shape of the truncated dome **b** modeled through MasterCAM software and **c** experimentally obtained from the SPIF test

during incremental forming [42–44]. In automobile applications, the surface roughness seriously affects the aesthetic appearance [2]. It majorly affects the smoothness and brilliance of the topcoat during the paint baking process. Also, when the part with higher surface roughness exposed to sudden loads, the service life of the component is greatly compromised. Hence, it is necessary to reduce the surface roughness of the material during deformation. Therefore, in the present work, the multi objective optimization technique of SPIF parameters was carried out to maximize the formability in terms of angle of failure (AF) and part depth per unit time (PDT) and to minimize the surface roughness of AA6061 sheet material.

### Design of experiments with response surface methodology

The response surface equation $Y$ can be represented by a quadratic polynomial as per Eq. (29).

$$Y = \beta_0 + \sum_{j=1}^{k} \beta_j x_j + \sum_{i=1}^{k} \beta_{jj} x_j^2 + \sum_{i=1}^{k-1} \sum_{j=i+1}^{k} \beta_{ij} x_i x_j + e \quad (29)$$

Here, $e$ represents a random error vector of the order of ($N \times 1$). For $N$ number of experiments, the response surface can be expressed as shown in Eq. (30).

$$Y = X\beta + e \quad (30)$$

Where,

$$Y = \begin{bmatrix} y_1 \\ y_2 \\ y_3 \\ \vdots \\ y_N \end{bmatrix}_{(N \times 1)}, X = \begin{bmatrix} 1 & x_{11} & x_{12} & \cdots & x_{1k} \\ 1 & x_{21} & x_{22} & \cdots & x_{2k} \\ 1 & x_{31} & x_{32} & \cdots & x_{3k} \\ \vdots & \vdots & \vdots & \ddots & \vdots \\ 1 & x_{N1} & x_{N2} & \cdots & x_{Nk} \end{bmatrix}_{(N \times k)},$$

$$\beta = \begin{bmatrix} \beta_1 \\ \beta_2 \\ \beta_3 \\ \vdots \\ \beta_k \end{bmatrix}_{(k \times 1)}, e = \begin{bmatrix} e_1 \\ e_2 \\ e_3 \\ \vdots \\ e_N \end{bmatrix}_{(N \times 1)}$$

Here, $\beta$ is the vector ($k \times 1$) of regression coefficients that need to be estimated. Also, Y is an output vector ($N \times 1$) and X is a ($N \times k$) matrix of the independent variables. The mathematical model is developed through regression analysis with analysis of variance (ANOVA) technique. In this work, the $F$ ratio [5] and corresponding probability ($p$) value are employed to check the significant term of the evaluated statistical model. The coefficient of determination ($R^2$) was also evaluated to find the goodness of the fit for the proposed regression model. Further, the correlations among the input process parameters were successfully established with the help of response surface methodology (RSM) technique, and Box-Behnken design (BBD) was successfully used to optimise the process parameters of SPIF process.

### Identification of the predominant process input parameters and responses

The input parameters are often termed as factors and the output variables are termed as responses. According to the trial results discussed in "Development of experimental setup and tool path planning" section, three independent process parameters, namely forming tool diameter (D), incremental step size (Z) and feed rate (FR) were identified as the primary influencing factors in the present study. The input factors with their unit, design levels, coded and un-coded forms are listed in Table 2. The number of experiments for the BBD was selected as $2k(k-1) + N_C = 15$ ($k$= number of factor = 3 and $N_C$= number of central points = 3). The mathematical computation was performed using statistical software, MINITAB (version 16) with the fifteen experiments based on three factors three levels BBD method.

Three different responses namely, angle of failure (AF), part depth per unit time (PDT), and surface roughness (SR) were measured from each fractured cone corresponding to each experimental condition. The procedure of measuring the angle of failure (AF) is explained schematically in Fig. 6a. For a fractured cone, five different points (P1 to P5) were identified along a curvilinear line as shown in Fig. 6b. The exact coordinate of these points was precisely measured using coordinate measuring machine (CMM). An imaginary best-fitted circle with center O was constructed with these five points. At point A, the angle subtended by the tangent AC with the horizontal plane is defined as the AF ($\theta$). The height (H) of the fractured truncated cone was also measured by CMM. Using this measurement, the AF was evaluated precisely, and the same was tabulated in "Regression analysis and optimization of the process parameters" section. Clearly, high AF indicated good formable SPIF condition. It is well known that SPIF is a comparatively slower process compared to conventional one [5]. Hence, one of the objectives of the current optimization is to reduce the duration of the process. Subsequently, part depth per unit time (PDT) was evaluated for each experimental condition following Eq. (31). Surface roughness is the imporarant response which was considered for the present work. A small area was cut at distance 15 mm from the top of the each truncated cone and the surface roughness of the specified area was evaluated with a Taylor Hobson 3D optical profilometer [45].

$$PDT = \frac{Height\ of\ the\ fractured\ dome\ (H)}{Total\ duration\ of\ forming\ process\ (T)} \quad (31)$$

### Regression analysis and optimization of the process parameters

Output variables or responses obtained from the SPIF experiments are listed in Table 3. These responses were further

**Table 2** Input SPIF process parameters with their maximum and minimum values

| Sl. No | Input parameters | Unit | Minimum value | | Middle value | | Maximum value | |
|---|---|---|---|---|---|---|---|---|
| | | | Un-coded | Coded | Un-coded | Coded | Un-coded | Coded |
| 1 | Tool Diameter (D) | mm | 4 | −1 | 7 | 0 | 10 | +1 |
| 2 | Step Size (Z) | mm | 0.2 | | 0.6 | | 1.0 | |
| 3 | Feed Rate (FR) | mm/min | 100 | | 500 | | 1000 | |

analyzed to determine the regression coefficients by establishing the mathematical relationships among the factors and responses. Separate regression models were developed for three responses using ANOVA technique. Accordingly, the best-fitted regression equations for all the responses are shown in Eq. (32) for the un-coded variables after removing the insignificant terms from the model. Also, the model performance index or $R^2$ value was evaluated from each of the ANOVA table. The AF, PDT and SR regression model fitness value in terms of $R^2$ were 0.9724, 0.9980 and 0.9627 respectively, which indicated that predicted model has a high fitness value towards the experimental data.

$$
\begin{aligned}
AF &= 72.290\text{-}1.611 \times D\text{-}3.264 \times Z\text{-}2.699 \times FR \\
&\quad +1.910 \times FR^2\text{-}1.617 \times D \times FR \\
PDT &= 2.0767\text{-}0.1972 \times D + 1.1483 \times Z + 1.5938 \\
&\quad \times FR\text{-}0.1563 \times D \times Z\text{-}0.1988 \times D \times FR \qquad (32) \\
&\quad +0.9620 \times Z \times FR \\
SR &= 3.145\text{-}1.117 \times D + 1.272 \times Z\text{-}0.943 \\
&\quad \times FR\text{-}1.060 \times D^2\text{-}1.327 \times D \times Z
\end{aligned}
$$

The SPIF process was optimized by setting different goals and priority to the responses. The weightage on the output variables was varied within 0.1–10 range and different importance (1, 2 and 3) was set based on the priority. In this work, the optimization was conducted imposing the weightage to the responses SR, AF, and PDT as 10, 1 and 0.1 respectively and prioritizing them as 1, 2 and 3 respectively. Most desirable process parameters for the SPIF process were tool diameter

(D) 4 mm, step size (Z) 0.2 mm and with a feed rate (FR) of 782 mm/min. Further, prediction of fracture locus and post forming analyses was conducted with a truncated dome prepared with the above mentioned optimized parameters.

# Results and discussion

## Prediction and validation of fracture locus of AA6061 sheet metal

### Experimental fracture forming limit diagram

Major and minor true strains of the deformed ellipses were plotted for different geometry specimens together. Experimental FLD is the tentative demarcation line between the safe and necking region as depicted by dotted line in Fig. 7. Further, the fracture strain at the principal locus ($\varepsilon_{1f}$, $\varepsilon_{2f}$) was estimated using the detailed experimental procedure as discussed in "Experiments to validate predicted fracture limit" section. Clearly, for each strain path, one pair of fracture strain ($\varepsilon_{1f}$, $\varepsilon_{2f}$) was evaluated for a single value of $\varepsilon_{2f}$. As repetitive PS tests were performed, a cluster of fracture data pair ($\varepsilon_{1f}$, $\varepsilon_{2f}$) was obtained for each strain path as shown in Fig. 7. Different coloured legend was used to distinguish among the fracture data pair resulted from different strain paths (SP1 to SP6). A tentative straight line just below the fracture data pairs was termed as an experimental fracture forming limit diagram (FFLD).

Further, the estimated FFLD was validated using the experimental fracture strain data points obtained from the



**Fig. 6** Measurement technique for angle of failure (AF) response **a** explained schematically and **b** corresponding fractured SPIF dome
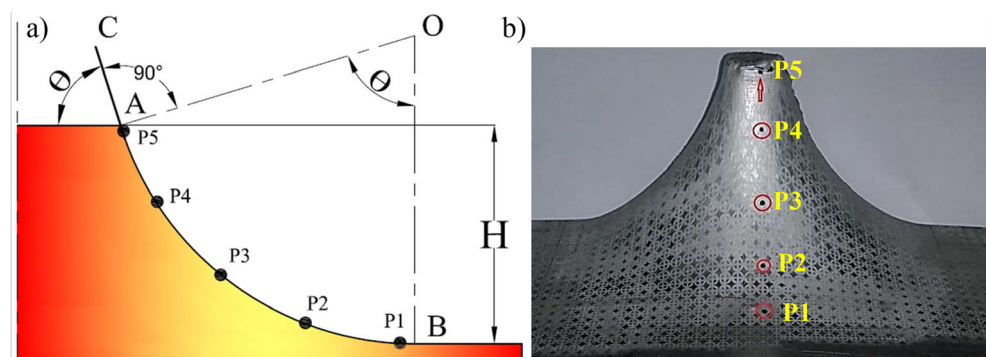
**Table 3** Responses measured after SPIF experiments according to the running sequence

| Std. Order | Run Order | Input process parameters | | | Response parameters | | |
|---|---|---|---|---|---|---|---|
| | | D (mm) | Z (mm) | FR (mm/min) | AF (°) | PDT (mm/min) | SR (μm) |
| 11 | 1 | 7 | 0.2 | 1000 | 75.60 | 1.50 | 2.37 |
| 7 | 2 | 4 | 0.6 | 1000 | 74.65 | 3.97 | 2.91 |
| 15 | 3 | 7 | 0.6 | 500 | 72.29 | 2.02 | 3.05 |
| 8 | 4 | 10 | 0.6 | 1000 | 69.54 | 3.18 | 1.12 |
| 2 | 5 | 10 | 0.2 | 500 | 75.11 | 0.69 | 1.45 |
| 14 | 6 | 7 | 0.6 | 500 | 72.29 | 2.24 | 3.12 |
| 9 | 7 | 7 | 0.2 | 100 | 81.27 | 0.16 | 4.02 |
| 12 | 8 | 7 | 1 | 1000 | 69.63 | 5.81 | 4.09 |
| 4 | 9 | 10 | 1 | 500 | 68.32 | 2.58 | 1.31 |
| 1 | 10 | 4 | 0.2 | 500 | 78.89 | 0.77 | 1.74 |
| 3 | 11 | 4 | 1 | 500 | 73.68 | 3.28 | 6.91 |
| 10 | 12 | 7 | 1 | 100 | 73.13 | 0.63 | 7.44 |
| 6 | 13 | 10 | 0.6 | 100 | 78.99 | 0.46 | 2.66 |
| 13 | 14 | 7 | 0.6 | 500 | 72.29 | 1.98 | 3.25 |
| 5 | 15 | 4 | 0.6 | 100 | 77.63 | 0.46 | 3.91 |

optimised fractured cup of SPIF process. It was noted that the failure mode during SPIF process was fracture without any hint of necking. Hence, the major and minor true strains from the fractured ellipses and nearby safe ellipses were measured from the optimised conical cup and correspondingly plotted in Fig. 7. It was further observed from the strain data that the strain path was nearly along the plane strain condition for this particular tool path. Correspondingly, the SPIF strain path was marked by a black arrowhead line as shown in the Fig. 7. It was also observed that the fracture points were well above from the evaluated FFLD and the safe points were below the fracture line. Hence, the estimated FFLD from punch stretching test was successfully validated by the SPIF test



**Fig. 7** Experimental FFLD obtained from punch stretching test and further validation with the experimental data obtained from optimized SPIF cup

results. Additionally, for each strain path, a pair of fracture strain locus ($\varepsilon_{1f}$, $\varepsilon_{2f}$) was identified. Correspondingly, for each fracture locus, the stress value and triaxiality parameters were evaluated which was further used to plot theoretical damage models as discussed in the next section.

## Prediction of limiting fracture strains using calibrated damage models

In the previous subsection, experimental FFLD was estimated and correspondingly validated with the SPIF test results. However, the experimental procedures for evaluating FFLD are laborious, resource consuming and demands sufficient expertise of the researcher to draw a reliable fracture line. Because of this reasons, an attempt was made in this work to estimate the experimental FFLD with the theoretical FFLD as discussed in "Ductile fracture criteria" section. As mentioned earlier, one destructive test (uniaxial tensile test) was performed to evaluate the seven different critical damage parameters. Correspondingly, the numerical values of critical damage parameters are enlisted in Table 4. For each strain path (SP1-SP6), effective fracture strain ($\overline{\varepsilon}_f^{Exp.}$) was estimated from the fracture data pair ($\varepsilon_{1f}$, $\varepsilon_{2f}$) of experimental FFLD using Eq. (6). Also, for each strain path, the effective fracture strain ($\overline{\varepsilon}_f^{Pred.}$) was predicted for various damage models using respective empirical relations as shown in the "Ductile fracture criteria" section. The estimated effective fracture strains ($\overline{\varepsilon}_f^{Pred.}$) were further decoupled along major ($\varepsilon_{1f}^{Pred.}$) and minor ($\varepsilon_{2f}^{Pred.}$) principal strain direction using Hill48 anisotropic yield theory as per Eq. (6). Here, Hill48 anisotropic yield model was indulged to predict the stress state, and correspondingly, stress triaxiality
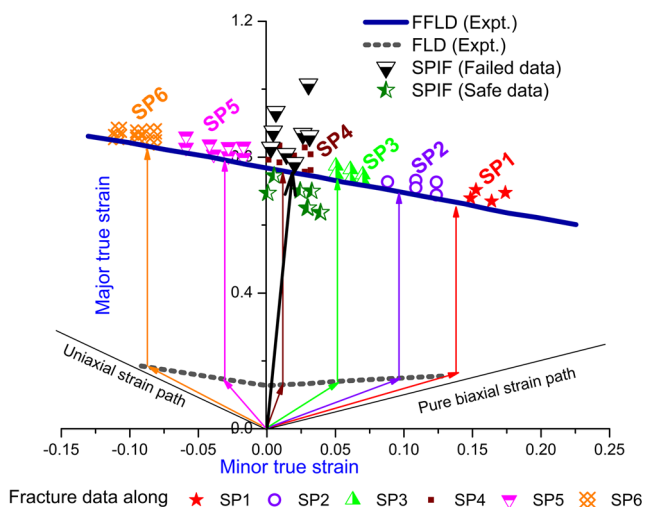
**Table 4** Material constants of various calibrated damage models obtained for AA6061 sheet

| Ductile fracture model | Abbr. | Damage parameters | Numerical value |
|---|---|---|---|
| Bao-Wierzbicki | BW | $C_{BW}$ | 0.5561 |
| Constant thickness strain based FFLD | CTFFLD | $C_{FFLD}$ | 0.8341 |
| Clift | CF | $C_{CF}$ | 348.50 |
| Cockcroft-Latham | CL | $C_{CL}$ | 348.52 |
| Oh | OH | $C_{OH}$ | 1.2194 |
| Brozzo | BR | $C_{BR}$ | 1.2190 |
| Rice-Tracey | RT | $C_{RT}$ | 0.5690 |

value ($\eta_{Hf}$) was estimated corresponding to all fracture strain points ($\varepsilon_{1f}$, $\varepsilon_{2f}$). Subsequently, a pair of triaxiality parameters ($\eta_{Hf}$, $L_{Pf}$) was obtained for every strain path.

In this work, the effective fracture strain ($\bar{\varepsilon}_f$) was predicted using different calibrated ductile damage models incorporating the anisotropy of the sheet material. Further, the FFLD was experimentally evaluated, and correspondingly, the effective fracture strain along each strain path was estimated using Hill48 anisotropy plasticity theory as per Eq. (6). All the experimental and predicted fracture strains along various strain paths were plotted in Fig. 8 for comparison purpose. Moreover, the fracture and safe data pair ($\varepsilon_1$, $\varepsilon_2$) was also converted into effective fracture strain and stress triaxiality locus ($\bar{\varepsilon}_f$, $\eta_H$) as shown in Fig. 8. Bao-Wierzbicki (BW) damage model estimated a reasonable prediction of effective fracture strains over the entire strain paths as observed from Fig. 8. In this work, it was observed that the thickness fracture strain varies along different strain path. Consequently, a considerably large variation in the fracture strain prediction was observed for the constant thickness strain based FFLD (CTFFLD) model. It is already highlighted in "Clift (CF) damage criterion" section that the Clift (CF) damage

model depends only on the material properties and independent of both $\eta_H$ and $L_P$. Hence, the estimated effective fracture strain ($\bar{\varepsilon}_f$) yielded a constant trend for CF model as depicted in Fig. 8. Cockcroft-Latham (CL) damage model was initially developed for a bulk forming operation like forging for the small and negative stress triaxiality regions. Hence, a large deviation was observed in predicted $\bar{\varepsilon}_f$ value as compared to that of the experimentally obtained effective fracture strains for high stress triaxiality region. Though Oh (OH) was a modified version of CL model, still the error in prediction was very high but slightly better than CL model. As Brozzo (BR) model included hydrostatic stress component into the model, the prediction was comparatively better than previous one. Still, the variation of calculated $\bar{\varepsilon}_f$ was higher over various strain paths. Rice-Tracey (RT) empirical model overpredicted the $\bar{\varepsilon}_f$. However, for designing a safe component in the manufacturing industry, it is always undesirable to use a damage model which over predicts the fracture strain. Further, it can be concluded from Fig. 8 that BW model gives the most reasonable prediction of $\bar{\varepsilon}_f$.

To add more insight into the variation of fracture strain, major fracture strains ($\varepsilon_{1f}$) along different strain path were estimated from the effective fracture strain ($\bar{\varepsilon}_f$) using Eq. (6). A straight line joining each of the major fracture strain data points along six different strain paths represented the estimated FFLD of that corresponding damage model as shown in Fig. 9. Experimental FFLD with the safe and fracture data points obtained from the SPIF test are also shown in the same figure. It is observed in Fig. 9 that six damage models such as CF, CL, OH, CTFFLD, BR and RT over-predict the major fracture limiting strain. However, the BW model predicts the major fracture strain more accurately. Hence, BW damage model turns out as an efficient damage model from uniaxial tension to equibiaxial tension region for AA6061 sheet metal.
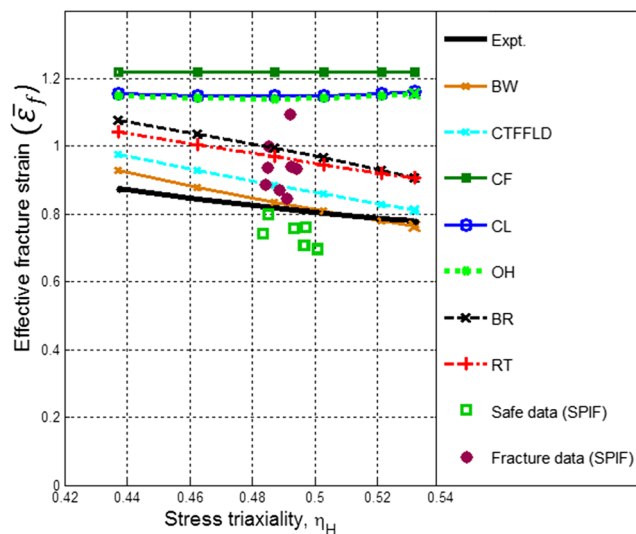
## Comparison of prediction efficiency of used damage models

Further, a comparative study was conducted to numerically estimate the prediction efficiency of each of the investigated
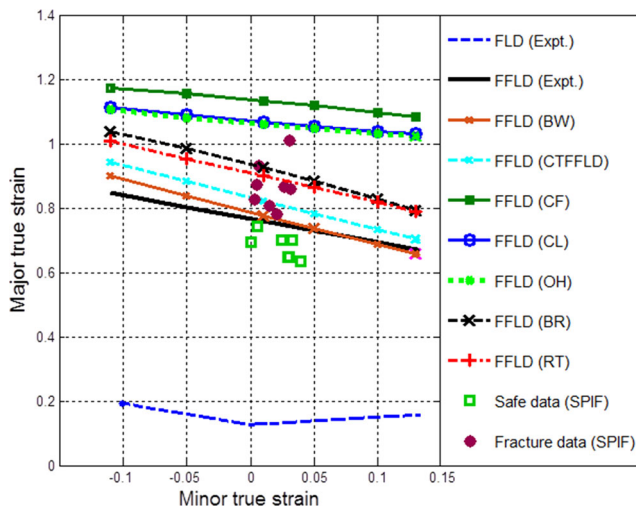


**Fig. 8** Comparison of various predicted fracture loci with optimized SPIF test data points in 2D anisotropy stress triaxiality space of ($\bar{\varepsilon}_f$, $\eta_H$)

**Fig. 9** Comparison of FFLDs predicted by various damage models along with optimized SPIF test data points

damage models. The efficiency of the theoretical models in terms of normalized absolute error (E value) was quantified by the parameter as shown in Eq. (33).

$$E_{SPi} = \left| \frac{\overline{\varepsilon}_f^{Exp.} - \overline{\varepsilon}_f^{Pred.}}{\overline{\varepsilon}_f^{Exp.}} \right|_{SPi} \times 100\%, \quad i = 1, 2, \ldots, 6. \quad (33)$$

The normalized absolute error (E) along different strain path is plotted in Fig. 10, and the corresponding average error ($E_{avg}$) in prediction is mentioned in parenthesis with each of the damage models. From Fig. 10, it is evident that $E_{avg}$ was least for BW damage model with a value of 2.71%. On contrary, CF criterion exhibits the lowest effective fracture strain prediction capability of the AA6061 alloy with an average error of 49.45%. Also, CTFFLD damage model is capable to predict the fracture strain within 8% average error level. Rest of the models, RT, BR, OH, and CL predict the fracture strain with a $E_{avg}$ value of
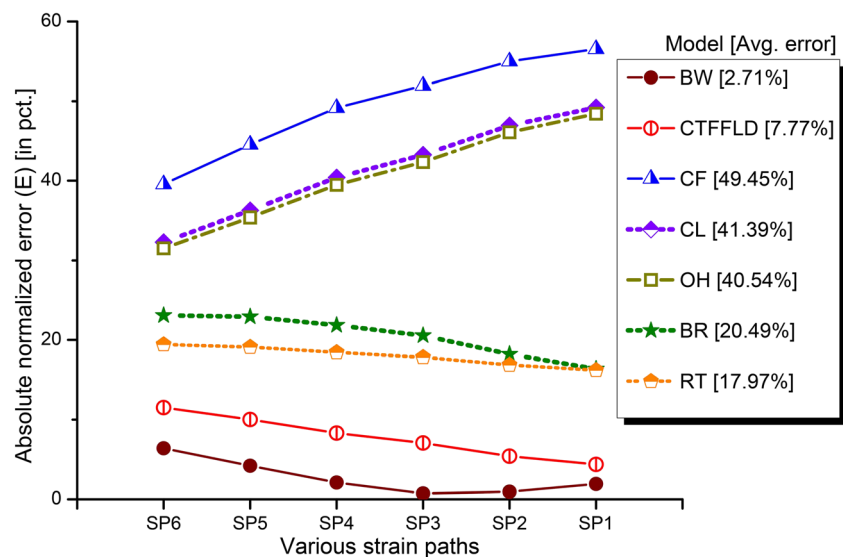
17.97%, 20.49%, 40.54% and 41.39% respectively. However, the error in prediction is not uniform as the strain path changes from SP6 to SP1. For low triaxiality region, the E value is small for the following models CF, CL, and OH, whereas the E value is remarkably increased in the high triaxiality region. On contrary, E value decreases at the higher triaxiality region for CTFFLD, BR and RT model. It is also observed that there is a considerable difference in the slope of the CTFFLD and experimental FFLD. For CTFFLD the slope is −1, whereas for experimental FFLD the value is −0.74. For this reason, at low triaxiality region (along SP6), the E value was more than 11% for CTFFLD model. Consequently, CTFFLD has not turned out to be an efficient fracture model in-spite of possessing an average error of 7.77%. For BW model E value exhibits no specific trend, but the model shows a satisfactory consistency in error prediction along the entire strain path, and also shows the least variation in E value combining all strain paths. Moreover, the BW model shows the maximum E value of 6.4% along any strain path. Hence, BW damage model is most suitable damage model, which is further exploited in 3D stress triaxiality space in next section.

### Effect of anisotropy on predicted fracture loci in 2D ($\eta$, $L_P$) and 3D ($\eta$, $L_P$, $\bar{\varepsilon}_f$) stress triaxiality space for selected damage models

In this subsection, the effect of anisotropy in the sheet material on the fracture locus was studied in 2D and 3D fracture space. The relation between stress triaxiality ratio ($\eta_H$) and Lode parameter ($L_P$) is represented by Eq. (8). Consequently, the variation of $\eta_H$ is shown in the Fig. 11 under plane stress condition ($\sigma_i=0$, where $i=1,2,3$ and $\sigma_1 \geq \sigma_2 \geq \sigma_3$) with different stress state clearly indicated inside the plot. The firm violet line at the top indicates the

**Fig. 10** Comparison of predictive accuracy of effective fracture strain for various ductile fracture models along different strain paths

Fig. 11 Effect of *r*-value on the stress triaxiality in the 2D space ($\eta$, $L_P$) with the SPIF working window of the present work (assuming $\sigma_1 \geq \sigma_2 \geq \sigma_3$)
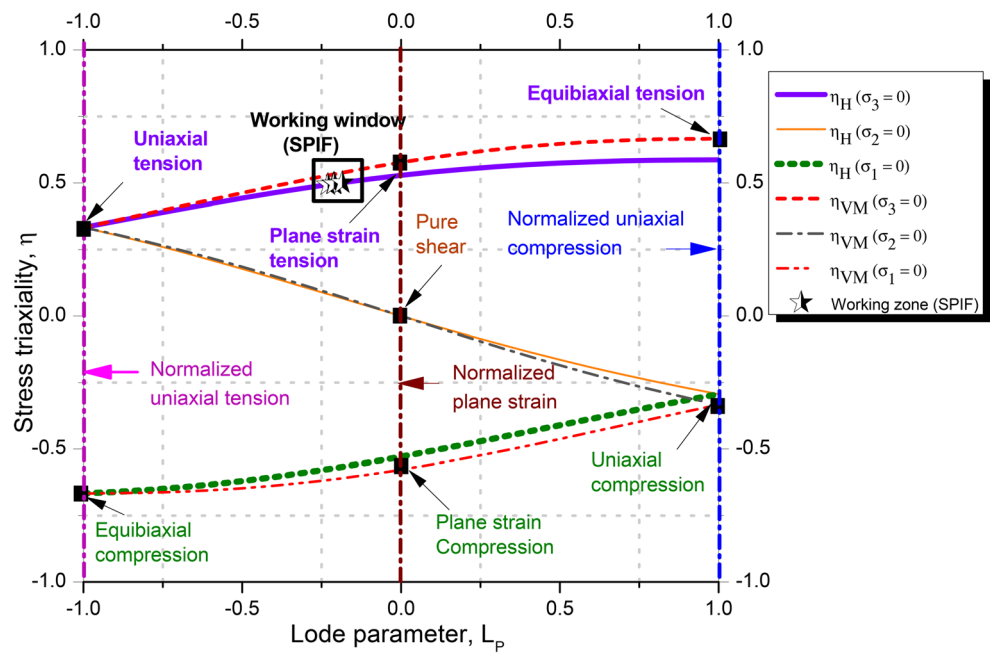
tension-tension stress state ($\sigma_1 > 0$, $\sigma_2 > 0$, $\sigma_3 = 0$) which represents sheet metal forming operation condition. The immediate yellow line indicates tension-compression stress state ($\sigma_1 > 0$, $\sigma_2 = 0$, $\sigma_3 < 0$) and last green dotted line represents compression-compression stress state ($\sigma_1 = 0$, $\sigma_2 < 0$, $\sigma_3 < 0$). Different intermediate points correspond to various test conditions. Further, the stress triaxiality evaluated through VM yield theory is also plotted in the same Fig. 11. It is already mentioned in "Hill48 anisotropy yield function" section, that if the *r*-value is imposed to be unity then Hill48 model leads to VM isotropic material model. In that condition, Eq. (8) is modified and the stress triaxiality ($\eta_{VM}$) variation with $L_P$ is plotted in the same figure. It is observed from Fig. 11 that at the equi-biaxial tension condition ($L_P = 1$, $\sigma_3 = 0$) the numerical values of stress triaxiality are $\eta_H = 0.587$ and $\eta_{VM} = 0.667$, and this variation reduces at normalized plane stress condition ($L_P = 0$, $\sigma_3 = 0$) with a value of $\eta_H = 0.528$ and $\eta_{VM} = 0.577$. Finally, at normalized uniaxial condition ($L_P = -1$, $\sigma_3 = 0$) both yield theory gives a constant value of stress triaxiality of 0.333. This concludes that sheet material anisotropy value influences the value of $\eta$ significantly. Further, the experimental fracture strain data ($\varepsilon_{1f}$, $\varepsilon_{2f}$) obtained from the optimized SPIF process is converted into triaxiality stress space ($\eta_H$, $L_P$) and marked as a working window at the tension-tension stress region as depicted in Fig. 11.

The fracture loci of the best predicted BW model is plotted in 3D stress triaxiality space to visualize the variation of the overall predictive capability of the model with anisotropy of the sheet material. 3D fracture locus for BW damage model is shown in Fig. 12 for sheet metal forming operation ($\sigma_3 = 0$). It can be observed that the BW locus is insensitive of $L_P$ as discussed in "Ductile fracture criteria" section. The red dot points correspond to the 2D fracture data points are obtained from optimized SPIF tests, and subsequently, are

converted into 3D locus using Hill48 anisotropy theory. If these 3D points are projected in the 2D ($\bar{\varepsilon}_f$, $\eta_H$) locus, then the SPIF fracture data points in Fig. 8 are obtained. Further, a considerable deviation is recorded in the 3D fracture locus predicted by both the Hill48 and VM theory. The plane stress locus ($\sigma_3 = 0$) is also shown in black and blue dotted points on the 3D fracture locus for Hill48 and VM yield theory respectively. Near the fracture SPIF data point location the effective fracture strain predicted by BW damage locus incorporating Hill48 and VM yield theory is 0.83 and 0.68 respectively. Clearly, for Hill48 model, the SPIF fracture points are in proximity to the BW fracture locus. Altogether it can be concluded that material anisotropy
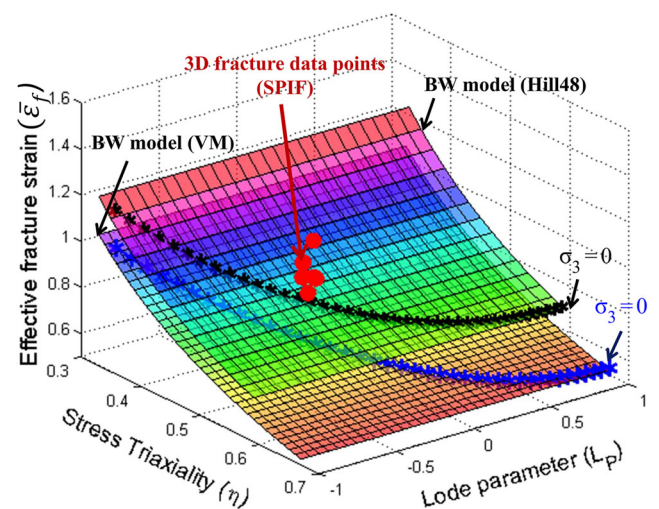


Fig. 12 Effect of *r*-value on the fracture locus of AA6061 sheet material calibrated by BW damage model with optimized SPIF test data points in 3D stress triaxiality space ($\eta$, $L_P$, $\bar{\varepsilon}_f$)

value (*r*-value) influence the stress triaxiality value considerably, which again affects the anisotropic ductile fracture criterion and consecutively the damage accumulation in the sheet metal. Hence, it is always advisable to incorporate anisotropy models to predict the effective fracture strain or critical damage parameter during the fracture prediction of anisotropic sheet material. In this work, the anisotropic Hill48 model was incorporated to predict the critical damage parameters and fracture strain. However, incorporation of advanced yield theory for prediction of various damage models is an interesting area of study and will be taken up as a future scope of this current work.

## Post-forming analysis

To get insight into the formability improvement and surface roughness during SPIF process, texture analysis was carried out. The microstructure evolution was correlated with these mechanical responses at the different location of the optimized truncated dome as elaborately discussed in the subsequent sections.

### Formability improvement during SPIF process

In aforementioned sections, it was found that the fracture limit of the material was higher compared to that of the necking limit. As a result, the maximum dome height of an optimized SPIF dome was 425% more than that of obtained from the PS tested dome along plane strain deformation mode. This is because of the two different deformation mechanism involved in the two different forming processes. For SPIF process, a small localized plastic deformation was produced by the hemispherical forming tool tip at the tool-workpiece contact point as shown in Fig. 4b. However, the formation of localized necking was hindered due to the inability of necks to grow around the circumferential bend path. Moreover, the material just surrounded to the deformation zone might be in considerably lower stress state which inhibited the crack growth at the deformation zone of the blank. On the other hand, the suppression of the localized necking was not occurred in punch stretching process due to uniform loading condition all over the deformable region on the blank. Unlike SPIF process, the difference in the stress state in the vicinity of plastically deformed zone might be comparatively less. Hence, the formability during SPIF process is always restricted by fracture without any hint of necking whereas in punch stretching mostly limited by necking.

To get insight into the non-uniform stress state during SPIF process, the texture analysis was performed on the optimized truncated cup. Four different locations were selected along the rolling direction on the fractured cup as shown in Fig. 13. First location (referred as a base point) was considered on the flange portion of the truncated cup where no deformation took place, and the other locations were selected at an interval of 20 mm

along the curvilinear path from the preceding location. The final location (referred as a critical point) was very near to the failed area of the optimized cup. The midpoint of the top flat undeformed portion of the truncated cone usually denoted as the pole. Clearly, different major plastic strains were induced in all the locations as mentioned in Table 5. It is well known that during deformation, the stored energy (yield response) of the grains changes with the crystallographic orientation. Taylor factor (TF) provides the yield response of individual grain that correlates to macroscopic deformation behaviour with microstructural characteristics of the material [46]. TF distribution maps were generated at predefined locations by the data set using the primary slip systems of {111} planes in the <110> direction inducing plane strain deformation gradient [46]. In TF maps, red-orange color coded grains represent the highest TF, whereas the blue-green intensity grains signify low TF value. According to Taylor plastic deformation theory [47], the grains with lower TF are considered to have suitable orientations for slip such that deformation proceeds easily whereas higher TF denotes that the occurrence of plastic deformation is difficult. This difficulty in plastic deformation arises due to high work hardening rate induced inside the grains [48]. It was observed from Fig. 13, that different levels of plastic deformation produced differential contribution of higher and lower TF grains. This resulted variation in the TF intensity denotes high discrepancy in the yield response of grains with deformation. Hence, to quantify nonuniformity in stress distribution with an increase in deformation, the volume fraction of high TF (red-orange) and low TF (blue-green) grains was measured using point counting approach of stereological methods [49] and correspondingly listed in Table 5.

At base point (location Q1), the volume fraction of grain with low TF was significantly higher in comparison to that of the grains with higher TF. This impressive presence of blue-green zone indicated the larger availability of suitable slip system for deformation. Further, it was inferred from Table 5 that with advancement in the deformation, the red-orange zone gradually increased which suggested the surge in work hardening rate. At location Q2, the blue-green zone decreased drastically in comparison to that of the initial base point or in other words the transition from low TF to moderate (yellow) TF zone took place at Q2. This indicated that further restricted deformation can be possible. With the increase in plastic deformation i.e. from location Q2 to location Q3, the grain appeared to be elongated with the appearance of fragmented grains. Also, the volume fraction of red-orange zone increased significantly to 45 from an initial condition of 31. Presence of the fragmented grains was also found in the critical point. However, the grains were found to be much more elongated compare to that of the location Q3. Besides, the volume fraction of high TF region was observed to be dominated at the Q4 location. This signified the occurrence of severe plastic deformation which ultimately leads to higher risk of catastrophic
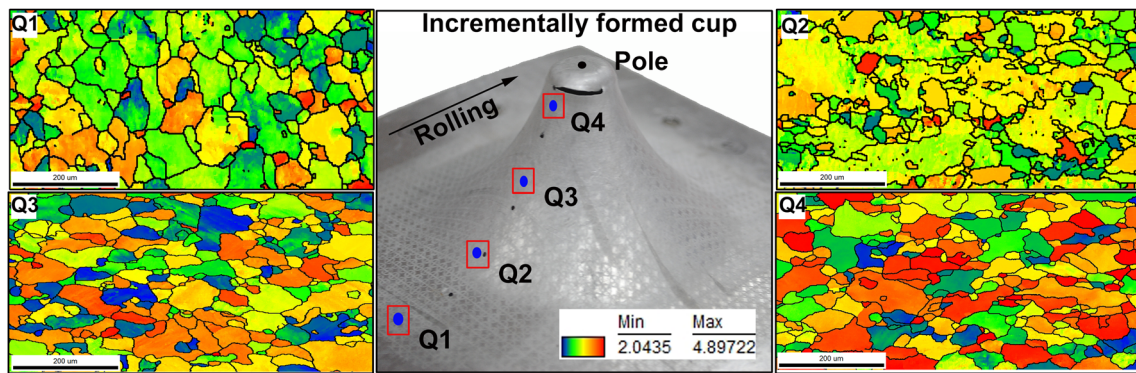
**Fig. 13** Taylor factor maps at different locations of the optimised incrementally formed cup

failure in the component at the vicinity of that designated region (Q4 location) [47]. Hence, the sudden fracture is always the failure mode of an incrementally formed cup. Further, localized stress ratio (Z) i.e. ratio of high TF to low TF grain was evaluated, and it was found that the value of Z increased remarkably while moving from base point (0.55) to a critical point (2.36). A steep decrease of the localized stress ratio from Q4 to Q3 confirmed the fact that the failure region was highly stressed compare to the nearby region. For this reason, the suppression of localized necking took place at tool-workpiece contact point during the SPIF process which helped to increase the formability of the material.

### Analysis of surface roughness profile

The areal average surface roughness value (Sa) of the optimized truncated cone was characterized at different major strain values (0, 0.29, 0.45, and 0.80) using a Taylor Hobson 3D optical profilometer. It was observed that the value increased significantly from 0.446 to 1.943 when progressively deformed from base point ($\varepsilon_1=0$) to critical point ($\varepsilon_1=0.8$). It was further observed that the larger the amount of deformation, more prominent was the surface roughness effect [50, 51]. The resulted undulations on the surface were due to the differential tendency of grain rotation during SPIF process of the sheet. In SPIF process, the roughness along the tool path rises significantly with plastic deformation. This is due to the

fact that during SPIF process, the material can only flow in one direction i.e. major strain direction whereas in other direction (transverse) deformation of the specimen is restrained. This restricted movement of the material and the crystalline slipping triggered the surface grains to rotate in the direction of the major principal strain, thus developing "trough" and "crest" on the free surface of the formed cup.

To correlate the evolution of texture with surface roughness, orientation distribution function (ODF) at $\Phi_2=0°$ and $65°$ sections were generated and analyzed by comparing with ideal texture components of FCC material as shown in Fig. 14b. It can be inferred from the Fig. 14c that in initial cold rolled condition, the cube and goss components were dominant with respect to that of brass, s, and rotated cube texture components. With the increase in plastic deformation, the contribution of brass and s texture components was found to be increased progressively. Being a low stacking fault FCC material, the increase in orientation density of brass component is expected under high deformation condition [52]. Further, the value of ODF intensities contour was found to be maximum at a major strain of 0.80 which signified that with the application of plastic deformation the grains rotated towards stable preferred orientation. At a critical point, dominating brass and s texture component with highest ODF intensity of 16.6 was observed. It was reported in the previous literature that order of the orientations from highest to lowest surface roughness is brass, s, cube, and goss texture component [53]. Thus, it can be inferred that the tremendous

**Table 5** The area percentage of different TF zones at the different strain level

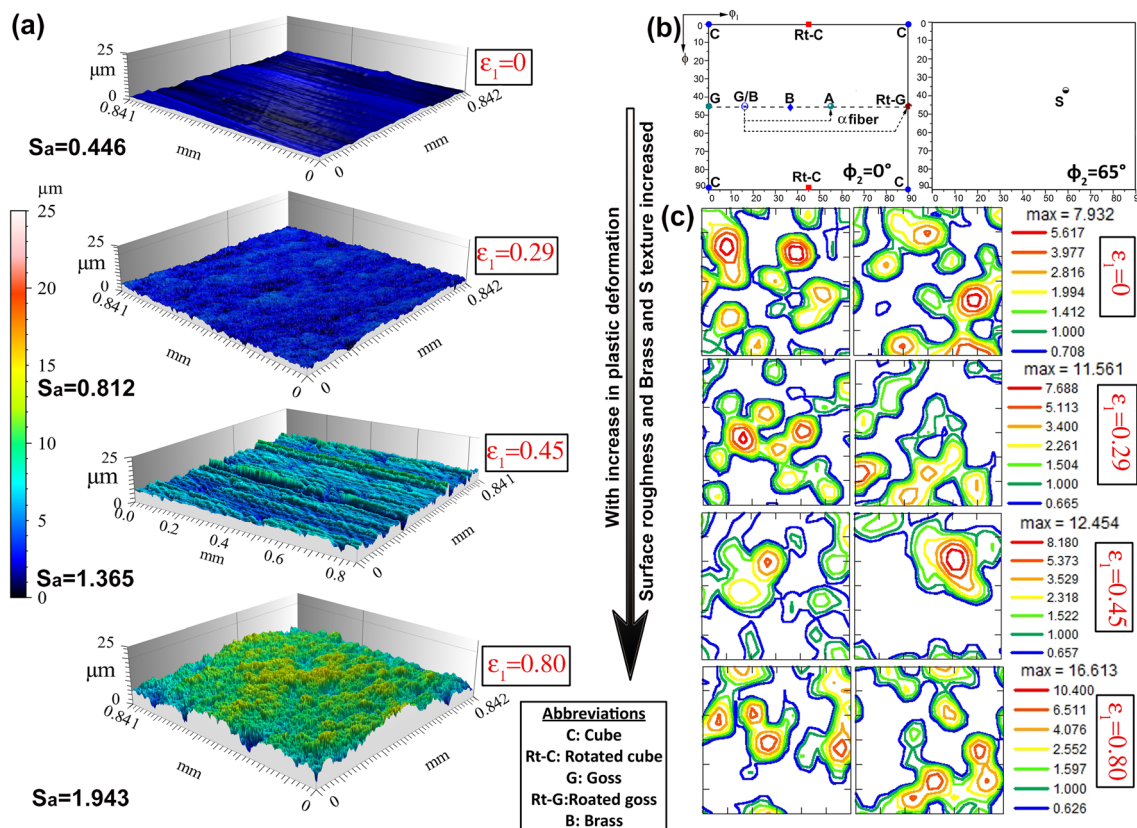| Deformed location | Major plastic strain | The area percentage of different zones (%) | | Localised stress ratio (Z = Y/X) |
|---|---|---|---|---|
| | | Blue-Green (X) | Red-Orange (Y) | |
| (Base point) Location Q1 | Undeformed | 56 | 31 | 0.55 |
| (Intermediate) Location Q2 | 0.29 | 31 | 38 | 1.23 |
| (Intermediate) Location Q3 | 0.45 | 26 | 45 | 1.73 |
| (Critical point) Location Q4 | 0.80 | 22 | 52 | 2.36 |

**Fig. 14** **a** Evolution of average surface roughness with major plastic strain, **b** schematic representation of the ideal texture component in FCC material at $\Phi_2=0°$ and $65°$ ODF section, and **c** evolution of texture with major plastic strain

increase in the brass and s texture component during SPIF process was responsible for the higher roughness value at higher strain levels. Hence, it can be concluded that the degree of roughening on the surface of the deformed cup are correlated with the grain rotation, which is a result of plastic deformation and crystallographic slip.

## Conclusions

In this work, single point incremental forming (SPIF) test setup was developed, and consequently, the optimized SPIF test and punch stretching (PS) test data were used to construct the experimental fracture forming limit diagram (FFLD) of AA6061 sheet metal. The theoretical fracture limit was predicted indulging Hill48 anisotropic yield theory coupling with seven various ductile fracture models, and the results were compared with the experimental data. The texture and surface roughness of the deformed cups were measured and analysed subsequently, and the major conclusions are listed below.

- The optimized parametric combination of tool diameter 4 mm, step size 0.2 mm and with a feed rate of 782 mm/min was used to fabricate a SPIF conical dome. Subsequently, the fracture strain locus, obtained from

optimized SPIF dome, was used to validate the experimental FFLD obtained from punch stretching (PS) test result. A massive 425% increase in maximum cup height was recorded in the incrementally formed dome compare to that of the PS tested dome along plane strain deformation path due to suppression of necking during SPIF test.

- Seven various ductile damage models were modified implementing the Hill48 plasticity theory to consider the influence of anisotropy on the effective fracture strain. Consequently, all the critical damage parameters were calibrated incorporating the material anisotropy value and the analytical fracture forming limit diagrams (FFLD) were also estimated. It was observed from 2D triaxiality locus ($\eta$, $L_P$) that incorporation of Hill48 anisotropy model reduced the $\eta$ value by 12% in equibiaxial condition and 8.5% in plane strain condition during sheet metal forming operation ($\sigma_3=0$). Also in 3D triaxiality locus ($\eta$, $L_P$, $\overline{\varepsilon}_f$), incorporation of $r$-value improved the effective fracture strain prediction by 18% in Bao-Wierzbicki (BW) model along plane strain condition.

- It was observed from the anisotropic effective strain locus ($\overline{\varepsilon}_f$, $\eta_H$) that six damage models, Clift (CF), Cockcroft-Latham (CL), Oh (OH), Constant thickness strain based FFLD (CTFFLD), Brozzo (BR), and Rice-Tracey (RT)

model over-predicted the effective fracture limiting strain which is most undesirable in practical application for designing a component. Further, two models, Bao-Wierzbicki (BW) and CTFFLD exhibited an average error of prediction less than 8%. Other five models, OH, CL, CF, BR and RT model displayed an average error of more than 17%. BW model showed the most encouraging predictive capability of fracture limit with an average absolute error of 2.71%. Hence, BW damage model can be considered as most efficient damage model to predict fracture in the AA6061 material during forming operation.

• Formability improvement in SPIF process in comparison to that of the conventional forming process was due to high stress gradient generated throughout the profile of SPIF truncated dome. Further, development of brass and s texture component with an increase in plastic deformation led to evolution in the average surface roughness value in the AA6061 material. Thus, the rate of surface roughness is found to be related to the grain rotation, which indeed, a consequence of plastic deformation and crystallographic slip.

## Compliance with ethical standards

**Conflict of interest** The authors declare that they have no conflict of interest.

**Publisher's Note** Springer Nature remains neutral with regard to jurisdictional claims in published maps and institutional affiliations.

## References

1. Voswinckel H, Bambach M, Hirt G (2015) Improving geometrical accuracy for flanging by incremental sheet metal forming. Int J Mater Form 8(3):391–399. https://doi.org/10.1007/s12289-014-1182-y

2. Jeswiet J, Micari F, Hirt G, Bramley A, Duflou J, Allwood J (2005) Asymmetric single point incremental forming of sheet metal. CIRP Ann Manuf Technol 54(2):88–114

3. Duflou JR, Verbert J, Belkassem B, Gu J, Sol H, Henrard C, Habraken AM (2008) Process window enhancement for single point incremental forming through multi-step toolpaths. CIRP Ann Technol 57(1):253–256

4. Lu B, Ou H, Shi SQ, Long H, Chen J (2016) Titanium based cranial reconstruction using incremental sheet forming. Int J Mater Form 9(3):361–370. https://doi.org/10.1007/s12289-014-1205-8

5. Bahloul R, Arfa H, Belhadjsalah H (2014) A study on optimal design of process parameters in single point incremental forming of sheet metal by combining box-Behnken design of experiments, response surface methods and genetic algorithms. Int J Adv Manuf Technol 74(1-4):163–185. https://doi.org/10.1007/s00170-014-5975-4

6. Isik K, Silva MB, Tekkaya AE, Martins PAF (2014) Formability limits by fracture in sheet metal forming. J Mater Process Technol 214(8):1557–1565. https://doi.org/10.1016/j.jmatprotec.2014.02.026

7. Martins PAF, Bay N, Tekkaya AE, Atkins AG (2014) Characterization of fracture loci in metal forming. Int J Mech Sci 83:112–123. https://doi.org/10.1016/j.ijmecsci.2014.04.003

8. Habibi N, Zarei-hanzaki A, Abedi H (2015) Journal of materials processing technology an investigation into the fracture mechanisms of twinning-induced-plasticity steel sheets under various strain paths. J Mater Process Technol 224:102–116. https://doi.org/10.1016/j.jmatprotec.2015.04.014

9. Abedini A, Butcher C, Worswick MJ (2017) Fracture characterization of rolled sheet alloys in shear loading: studies of specimen geometry, anisotropy, and rate sensitivity. Exp Mech 57(1):75–88. https://doi.org/10.1007/s11340-016-0211-9

10. Bai Y, Wierzbicki T (2015) A comparative study of three groups of ductile fracture loci in the 3D space. Eng Fract Mech 135:147–167. https://doi.org/10.1016/j.engfracmech.2014.12.023

11. Park N, Huh H, Lim SJ, Lou Y, Kang YS, Seo MH (2017) Fracture-based forming limit criteria for anisotropic materials in sheet metal forming. Int J Plast 96:1–35. https://doi.org/10.1016/j.ijplas.2016.04.014

12. McAnulty T, Jeswiet J, Doolan M (2017) Formability in single point incremental forming: a comparative analysis of the state of the art. CIRP J Manuf Sci Technol 16:43–54. https://doi.org/10.1016/j.cirpj.2016.07.003

13. Fiorentino A, Marzi R, Ceretti E (2012) Preliminary results on Ti incremental sheet forming (ISF) of biomedical devices: biocompatibility, surface finishing and treatment. International Journal of Mechatronics and Manufacturing Systems 5(1):36–45. https://doi.org/10.1504/IJMMS.2012.046146

14. Feng JW, Zhan LH, Yang YG (2016) The establishment of surface roughness as failure criterion of Al–Li alloy stretch-forming process. Metals 6(1):13. https://doi.org/10.3390/met6010013

15. Hill R (1948) A theory of the yielding and plastic flow of anisotropic metals. Proc R Soc Lond A 193(1033):281–297. https://doi.org/10.1098/rspa.1948.0045

16. Basak S, Panda SK (2016) Application of Barlat Yld-96 Yield Criterion for Predicting Formability of Pre-Strained Dual Phase Steel Sheets. In: ASME 2016 11th International Manufacturing Science and Engineering Conference. p V001T02A063–V001T02A063

17. Basak S, Panda SK, Zhou YN (2015) Formability assessment of Prestrained automotive grade steel sheets using stress based and polar effective plastic strain-forming limit diagram. J Eng Mater Technol 137(4):041006. https://doi.org/10.1115/1.4030786

18. Bai Y, Wierzbicki T (2008) A new model of metal plasticity and fracture with pressure and lode dependence. Int J Plast 24(6):1071–1096. https://doi.org/10.1016/j.ijplas.2007.09.004

19. Bao Y, Wierzbicki T (2004) On fracture locus in the equivalent strain and stress triaxiality space. Int J Mech Sci 46(1):81–98. https://doi.org/10.1016/j.ijmecsci.2004.02.006

20. Lee YW (2005) Fracture prediction in metal sheets (PhD thesis). Massachusetts Institute Of Technology, Cambridge, United States

21. Considere A (1885) Use of the iron and steel in buildings. Ann Des Ponts Chaussees 9:574–575

22. Gorji M, Berisha B, Hora P, Barlat F (2015) Modeling of localization and fracture phenomena in strain and stress space for sheet metal forming. Int J Mater Form. https://doi.org/10.1007/s12289-015-1242-y

23. Silva MB, Nielsen PS, Bay N, Martins PAF (2011) Failure mechanisms in single-point incremental forming of metals. Int J Adv Manuf Technol 56(9-12):893–903. https://doi.org/10.1007/s00170-011-3254-1

24. Freudenthal AM (1950) The inelastic behavior of solids. Wiley, New York

25. Clift SE, Hartley P, Sturgess CEN, Rowe GW (1990) Fracture prediction in plastic deformation processes. Int J Mech Sci 32(1):1–17. https://doi.org/10.1016/0020-7403(90)90148-C

26. Cockcroft MG, Latham DJ (1968) Ductility and the workability of metals. J Inst Met 96:33–39

27. Tarigopula V, Hopperstad OS, Langseth M, Clausen AH, Hild F, Lademo OG, Eriksson M (2008) A study of large plastic deformations in dual phase steel using digital image correlation and FE analysis. Exp Mech 48(2):181–196. https://doi.org/10.1007/s11340-007-9066-4

28. Oh SI, Chen CC, Kobayashi S (1979) Ductile fracture in axisymmetric extrusion and drawing-part 2: workability in extrusion and drawing. Journal of Engineering for Industry 101(1):36–44. https://doi.org/10.1115/1.3439471

29. Brozzo P, Deluca B, Rendina R (1972) A new method for the prediction of formability in metal sheets, sheet material forming and formability. In: Proceedings of the Seventh Biennial Conference of the IDDRG

30. Rice JR, Tracey DM (1969) On the ductile enlargement of voids in triaxial stress fields∗. J Mech Phys Solids 17(3):201–217. https://doi.org/10.1016/0022-5096(69)90033-7

31. Nakazima K, Kikuma T, Hasuka K (1968) Study on the formability of steel sheets. Yawata Tech Rep 264:8517–8530

32. Basak S, Panda SK (2018) Implementation of Yld96 anisotropy plasticity theory for estimation of polar effective plastic strain based failure limit of pre-strained thin steels. Thin-Walled Struct 126:26–37

33. Dhara S, Basak S, Panda SK, Hazra S, Shollock B, Dashwood R (2016) Formability analysis of pre-strained AA5754-O sheet metal using Yld96 plasticity theory: role of amount and direction of uniaxial pre-strain. J Manuf Process 24:270–282. https://doi.org/10.1016/j.jmapro.2016.09.014

34. Prasad KS, Panda SK, Kar SK et al (2017) Microstructures, forming limit and failure analyses of Inconel 718 sheets for fabrication of aerospace components. J Mater Eng Perform 26(4):1513–1530

35. Panicker SS, Prasad KS, Basak S, Panda SK (2017) Constitutive behavior and deep Drawability of three aluminum alloys under different temperatures and deformation speeds. J Mater Eng Perform 26(8):3954–3969

36. Prasad KS, Gupta AK, Singh Y, Singh SK (2016) A modified mechanical threshold stress constitutive model for austenitic stainless steels. J Mater Eng Perform. https://doi.org/10.1007/s11665-016-2389-5

37. Gatea S, Ou H, McCartney G (2016) Review on the influence of process parameters in incremental sheet forming. Int J Adv Manuf Technol 87(1-4):479–499. https://doi.org/10.1007/s00170-016-8426-6

38. Emmens WC, Sebastiani G, van den Boogaard AH (2010) The technology of incremental sheet forming-a brief review of the history. J Mater Process Technol 210(8):981–997. https://doi.org/10.1016/j.jmatprotec.2010.02.014

39. Behera AK, de Sousa RA, Ingarao G, Oleksik V (2017) Single point incremental forming: an assessment of the progress and technology trends from 2005 to 2015. J Manuf Process 27:37–62

40. Silva MB, Skjoedt M, Atkins a G et al (2008) Single-point incremental forming and formability–failure diagrams. J Strain Anal Eng Des 43(1):15–35. https://doi.org/10.1243/03093247JSA340

41. Madeira T, Silva CMA, Silva MB, Martins PAF (2015) Failure in single point incremental forming. Int J Adv Manuf Technol 80(9-12):1471–1479. https://doi.org/10.1007/s00170-014-6381-7

42. Hagan E, Jeswiet J (2004) Analysis of surface roughness for parts formed by computer numerical controlled incremental forming. Proc Inst Mech Eng B J Eng Manuf 218(10):1307–1312

43. Hamilton K, Jeswiet J (2010) Single point incremental forming at high feed rates and rotational speeds: surface and structural consequences. CIRP Ann Manuf Technol 59(1):311–314. https://doi.org/10.1016/j.cirp.2010.03.016

44. Durante M, Formisano A, Langella A (2010) Comparison between analytical and experimental roughness values of components created by incremental forming. J Mater Process Technol 210(14):1934–1941

45. Bennett JM (1992) Recent developments in surface roughness characterization. Meas Sci Technol 3(12):1119

46. Prasad KS, Panda SK, Kar SK, Murty SVSN, Sharma SC (2018) Effect of solution treatment on deep drawability of IN718 sheets: experimental analysis and metallurgical characterization. Mater Sci Eng A 727:97–112. https://doi.org/10.1016/j.msea.2018.04.110

47. Masoumi M, Santos LPM, Bastos IN, Tavares SSM, da Silva MJG, de Abreu HFG (2016) Texture and grain boundary study in high strength Fe-18Ni-co steel related to hydrogen embrittlement. Mater Des 91:90–97. https://doi.org/10.1016/j.matdes.2015.11.093

48. Goel S, Jayaganthan R, Singh IV, Srivastava D, Dey GK, Saibaba N (2015) Texture evolution and ultrafine grain formation in cross-cryo-rolled zircaloy-2. Acta Metallurgica Sinica (English Letters) 28(7):837–846. https://doi.org/10.1007/s40195-015-0267-z

49. Weibel ER (1989) Measuring through the microscope: development and evolution of stereological methods. J Microsc 155(3):393–403

50. Osakada K, Oyane M (1971) On the roughening of free surface in deformation processes. Bulletin of JSME 14(68):171–177

51. Dai K, Villegas J, Shaw L (2005) An analytical model of the surface roughness of an aluminum alloy treated with a surface nanocrystallization and hardening process. Scr Mater 52(4):259–263. https://doi.org/10.1016/j.scriptamat.2004.10.021

52. Savoie J, Zhou Y, Jonas JJ, Macewen SR (1996) Textures induced by tension and deep drawing in aluminum sheets. Acta Mater 44(2):587–605. https://doi.org/10.1016/1359-6454(95)00214-6

53. Rossiter J, Brahme A, Inal K, Mishra R (2013) Numerical analyses of surface roughness during bending of FCC single crystals and polycrystals. Int J Plast 46:82–93. https://doi.org/10.1016/j.ijplas.2013.01.016